

1 **4D live-cell imaging of microgametogenesis in the human malaria**
2 **parasite *Plasmodium falciparum***

3 Sabrina Yahiya¹, Sarah Jordan¹, Holly X. Smith¹, David C. A. Gaboriau², Mufuliat T.
4 Famodimu¹, Farah A. Dahalan¹, Alisje Churchyard¹, George W. Ashdown^{1,3} and Jake
5 Baum^{1*}

6

7 ¹ Department of Life Sciences and ² Facility for Imaging by Light Microscopy, Imperial
8 College London, Sir Alexander Fleming Building, Exhibition Road, South Kensington,
9 London, SW7 2AZ, UK.

10 ³ Walter and Eliza Hall Institute of Medical Research, Parkville, Victoria, Australia.

11

12 ***Correspondence to:**

13 Jake Baum (jake.baum@imperial.ac.uk), Department of Life Sciences, Imperial College
14 London, Exhibition Road, South Kensington, London SW7 2AZ, United Kingdom.

15 **Key words:**

16 *Plasmodium falciparum*; microgametogenesis; exflagellation; transmission; parasite biology;
17 time-lapse imaging; microscopy; drug discovery; drug phenotype.

18 **ABSTRACT**

19 Formation of gametes in the malaria parasite occurs in the midgut of the mosquito and is
20 critical to onward parasite transmission. Transformation of the male gametocyte into
21 microgametes, called microgametogenesis, is an explosive cellular event and one of the
22 fastest eukaryotic DNA replication events known. The transformation of one
23 microgametocyte into eight flagellated microgametes requires reorganisation of the parasite
24 cytoskeleton, replication of the 22.9 Mb genome, axoneme formation and host erythrocyte
25 egress, all of which occur simultaneously in <20 minutes. Whilst high-resolution imaging has
26 been a powerful tool for defining stages of microgametogenesis, it has largely been limited to
27 fixed parasite samples, given the speed of the process and parasite photosensitivity. Here,
28 we have developed a live-cell fluorescence imaging workflow that captures the explosive
29 dynamics of microgametogenesis in full. Using the most virulent human malaria parasite,
30 *Plasmodium falciparum*, our live-cell approach combines three-dimensional imaging through
31 time (4D imaging) and covers early microgametocyte development through to microgamete
32 release. Combining live-cell stains for DNA, tubulin and the host erythrocyte membrane, 4D
33 imaging enables definition of the positioning of newly replicated and segregated DNA. It also
34 shows the microtubular cytoskeleton, location of newly formed basal bodies and elongation
35 of axonemes, as well as behaviour of the erythrocyte membrane, including its specific
36 perforation prior to microgamete egress. 4D imaging was additionally undertaken in the
37 presence of known transmission-blocking inhibitors and the untested proteasomal inhibitor
38 bortezomib. Here, for the first time we find that bortezomib inhibition results in a clear block
39 of DNA replication, full axoneme nucleation and elongation. These data not only define a
40 framework for understanding microgametogenesis in general but also suggest that the
41 process is critically dependent on proteasomal activity, helping to identify potentially novel
42 targets for transmission-blocking antimalarial drug development.

43 INTRODUCTION

44 Malaria disease is caused by single-cell protozoan parasites from the genus *Plasmodium*.
45 Over its complex two-host lifecycle, the *Plasmodium* cell demonstrates remarkable cellular
46 plasticity as it transitions between multiple developmental stages. In the transition from
47 mammalian to mosquito host, the parasite faces an extreme population bottleneck in
48 numbers, which also presents a natural target for novel antimalarial treatments aimed at
49 blocking transmission. Transmission is triggered by the uptake of sexual stage gametocytes
50 during a mosquito feed that instantly activate, initiating a transformation in the mosquito
51 midgut that has become a trademark in the cellular biology of these protozoan parasites¹.

52 Dormant male (micro) and female (macro) gametocytes form a sub-population of between
53 0.2-1% of the circulating asexual blood stage parasite reservoir in the mammalian host. The
54 signals that initiate commitment of asexual parasites to sexual differentiation are, however,
55 poorly understood¹. Committed gametocytes mature over five distinct morphological stages
56 (referred to as stages I-V) and are believed to sequester in the host bone marrow and
57 spleen, before emerging into the bloodstream when they reach stage V maturity¹⁻³. Following
58 ingestion by a feeding mosquito, stage V microgametocytes and macrogametocytes
59 transform rapidly to microgametes and macrogametes, respectively. The transformation from
60 gametocyte to gamete, a process termed gametogenesis, is activated by a decrease in
61 temperature to 20-25°C, rise in pH and the presence of the mosquito metabolite, xanthurenic
62 acid in the mosquito midgut⁴.

63 *Plasmodium* gametogenesis is distinctly different between male and female parasites. Both
64 entail a morphological change from falciform to rounded, in *P. falciparum*, and egress from
65 within the host erythrocyte by an ‘inside-out’ mechanism. This mechanism of egress involves
66 disintegration of the parasitophorous vacuole membrane (PVM) prior to that of the host
67 erythrocyte⁵. The female macrogametocyte rounds up⁶ and egresses⁷ within 10 minutes of
68 activation, emerging as a fertilisation competent macrogamete. Whilst this process is
69 incompletely understood, reverse genetic studies using different *Plasmodium* species have

70 described some key female specific events underlying macrogametogenesis⁸⁻¹², such as
71 release of osmiophilic bodies, membrane-bound organelles which are sparse if not entirely
72 absent in microgametocytes¹³. Whilst females become fertilisation-competent upon egress
73 and undergo little cellular reorganisation beyond rounding, microgametogenesis is
74 notoriously complex, and is the focus of our study here.

75 Microgametogenesis has been most extensively studied by electron microscopy (EM)
76 investigation of the rodent malaria parasite, *P. berghei* and *P. yoelii*.¹⁴⁻¹⁶ The detailed EM
77 work has revealed that microgamete formation entails a stepwise series of events including:
78 substantial cytoskeletal rearrangement, three rounds of DNA replication, alternating with
79 three rounds of endomitotic division, all of which occurs in ~15-20 minutes. *P. falciparum*
80 gametocytes start as falciform, a characteristic from which the species derives its name^{2,3},
81 before morphologically transforming to round once activated. Upon activation, a single
82 microtubule organising centre (MTOC) has been shown to transform into two orthogonal
83 tetrads of basal bodies attached to a spindle pole. The resulting eight basal bodies, from
84 which eight axonemes nucleate and elongate, segregate with each endomitotic
85 division^{15,17,18}. Axoneme assembly occurs, fuelled by the large quantities of tubulin within
86 mature microgametocyte that rapidly polymerises to form microtubules¹⁹. Prior to activation,
87 the MTOC starts in close alignment with the nuclear pore, permitting each basal body to pull
88 a haploid genome (1n) from the newly replicated octoploid (8n) genome through the parental
89 cell body at the point of emergence¹⁵. This dynamic process by which developing haploid
90 microgametes emerge as motile flagellar is a process termed exflagellation and occurs from
91 ~15 minutes post-activation¹⁷. Motile haploid microgametes then fuse with the sessile
92 macrogamete, producing a motile zygote able to migrate to the midgut epithelium for oocyst
93 formation and onwards progression in the mosquito²⁰.

94 Current insights into the processes of male and female gametogenesis have taken
95 advantage of the high temporal and spatial resolution offered by brightfield and fluorescence
96 imaging, respectively^{21,22}. However, microtubules are not easily resolvable by brightfield and

97 the specificity of fluorescent imaging often requires antibody staining, limiting imaging to
98 fixed samples. This is also true for electron microscopy, despite its proven utility in shaping
99 our current understanding of the fine cellular biology of microgametogenesis^{14,15,23}. As a
100 result, the dynamic nature of events encompassing microgametogenesis are still very poorly
101 understood. Better temporal characterisation using live samples, coupled with the specificity
102 of fluorescently tagged structures would allow a marked improvement in our understanding
103 of the process of microgametogenesis and provide a platform from which strategies to block
104 it might then be translatable.

105 Low and high-resolution microscopy of *Plasmodium* has been extensively used to
106 understand the cell biology of parasite development and aid drug-intervention studies.
107 Ultrastructure expansion microscopy was recently shown to advance traditional fluorescence
108 microscopy approaches to fixed parasite imaging, allowing close observation of asexual
109 blood stage, microgametocyte and ookinete cytoskeletal development²². A recent study
110 reported the application of semi-supervised machine learning to define asexual parasite
111 development in a high-throughput imaging format, using fixed parasites²⁴. The study proved
112 to be a powerful tool in detecting parasites with morphological perturbations when treated
113 with known antimalarials²⁴. Another recent high throughput screen reported the phenotypes
114 of transmission blocking antimalarial hits with unknown cellular targets²⁵. The study utilised
115 immunofluorescence labelling of fixed parasites undergoing microgametogenesis to
116 manually define cellular phenotypes. The same screen utilised low-resolution, live brightfield
117 imaging of exflagellation in a high-throughput assay²¹ to identify the microgametogenesis-
118 blocking hits²⁵. Live-cell fluorescence microscopy has also been explored, with a recent
119 study utilising lattice light-sheet microscopy to acquire 3D live time-lapse data of asexual *P.*
120 *falciparum* invasion²⁶. Other studies have reported the use of live-cell fluorescence imaging
121 of microgametogenesis to define the phenotypes of transgenic *P. berghei*^{27,28} cell lines.
122 Given the error prone nature of microgametogenesis¹⁶, however, it is important to define true

123 perturbations to microgametogenesis over natural variation and, critically, to do so in real
124 time.

125 Here, we describe a protocol that enables the labelling of microtubules, DNA and host
126 erythrocyte membrane for *P. falciparum* microgametocytes and their imaging by live-cell 3D
127 fluorescence microscopy (4D imaging), capturing the entire process of microgametogenesis.

128 To develop a workflow that is translatable to other research labs, we have used a
129 combination of widefield microscopy, an open-source analysis software for deconvolution
130 and commercially available reagents throughout this study. Using this approach, we define in
131 detail the dynamic morphological transformations that occur during microgametogenesis,
132 from activation through to exflagellation. Furthermore, we demonstrate the applicability of
133 our protocol to phenotypic characterisation of inhibitors of microgametogenesis, in particular
134 the role of the proteasome, demonstrating the power of this approach for future
135 transmission-blocking drug discovery²⁴.

136 **RESULTS**

137 **Development of a live microgametogenesis 4D imaging approach**

138 To date, visualisation of the complex cytoskeletal rearrangement, host erythrocyte egress
139 and DNA replication events during *P. falciparum* microgametogenesis (**Figure 1A**) has
140 mostly been limited to fixed imaging protocols. We set out to devise a live cell imaging
141 workflow (**Figure 1B**) that permits observation of cellular dynamics during
142 microgametogenesis in real-time and in three dimensions (4D imaging). Selective testing of
143 several dyes revealed that the silicon-rhodamine (SiR) derivative SiR-tubulin, Vybrant™
144 DyeCycle™ Violet and wheat germ agglutinin (WGA) combined to effectively stain live
145 microgametocyte microtubules, DNA and the host erythrocyte membrane, respectively. SiR-
146 tubulin, a non-toxic far-red fluorogenic probe²⁹, is an SiR-derivative conjugated to
147 docetaxel³⁰ which binds specifically to microtubules and we demonstrate its specificity and
148 photostability in live cell fluorescence imaging of microgametogenesis. Vybrant™
149 DyeCycle™ Violet is a cell permeable dye which binds to double-stranded DNA to emit a
150 fluorescent signal proportional to DNA mass and has been previously used to measure
151 microgametocyte genome replication during microgametogenesis^{31,32} using flow cytometry.
152 Stage V gametocytes from the *P. falciparum* NF54 strain, were cultured as previously
153 described³³, stained and strictly maintained at 37°C to prevent premature activation of
154 gametogenesis. Gametogenesis was initiated by mimicking conditions of the mosquito
155 midgut using “ookinete media” (see Materials and Methods), a xanthurenic-acid-containing
156 media maintained at pH 7.4 and used at room temperature (RT). Labelled gametocytes were
157 directly added to ookinete media-containing imaging slides and prepositioned on the
158 microscope for the immediate acquisition of time-lapse data (**Figure 1B**).
159 To visualise the initial developmental stages of microgametogenesis, microgametocytes
160 were identified by SiR-tubulin-stained mitotic spindles which signified a successful round of
161 DNA replication (**Figure 1A**). Due to the rapid turnaround between activation and DNA
162 replication, most time-lapses presented here were acquired from 1-2 minutes-post activation,

163 following a round of replication. In optimisation of the imaging workflow, we found the
164 alternation between fluorescence and brightfield acquisition to significantly maximise the
165 viability of microgametocytes. Following identification of an activated microgametocyte, 3-
166 colour fluorescent time-lapses were immediately acquired before switching to brightfield
167 microscopy. A maximum of 10 frames were acquired in fluorescence to minimise the
168 phototoxic effects and brightfield microscopy was subsequently used to monitor parasite
169 development. Upon observation of further parasite differentiation in brightfield, for example
170 by rounding up or preparing for egress, image acquisition was switched back to fluorescence
171 for further acquisition of time-lapses to capture the full early developmental stages of
172 microgametogenesis.

173 Despite best efforts to reduce LED intensity and frame rates, phototoxicity nearly always
174 prevented the complete visualisation of microgametogenesis from start to finish. To
175 circumvent this issue, activated microgametocytes were imaged at different stages to ensure
176 full capture of later developmental stages, specifically the emergence of microgametes
177 during exflagellation (**Figure 1A**). In this late-stage instance, viable microgametocytes were
178 identified based on SiR-tubulin-stained axonemes, coiled around the parasite cell body.
179 Whilst the earlier stages of microgametogenesis were acquired in 4D, through Z and T,
180 exflagellation could only be captured as single Z-slice time-lapses given the dynamic nature
181 of emerging microgametes (**Figure 1B**). Time-lapse data of the early and later stages of
182 microgametogenesis were subsequently combined and could be analysed together, enabling
183 us to dissect microgametogenesis in its entirety, from initial endomitotic division through to
184 microgamete emergence, for the first time.

185

186 **Insights into cytoskeletal rearrangements during microgametogenesis**

187 The formation of mitotic spindles, basal bodies and axonemes occurs with rapid succession
188 during the early stages of microgametogenesis^{15,16}. Using our 4D imaging platform we
189 sought to define these stages in real time.

190 As depicted in **Figures 2A-C**, the mitotic spindle of a developing microgametocyte first
191 formed and lengthened across the width of the parasite. Consistent with existing knowledge
192 of microgametogenesis, mitotic spindle formation started out as a single MTOC that then
193 transformed into two tetrads of basal bodies upon the first round of DNA replication (**Figure**
194 **1A** and **Supplementary Video 1**). Axonemes were then seen to nucleate from each basal
195 body and subsequently elongated, coiling around the parasite, as shown in **Figures 2A-D**
196 and **Supplementary Videos 1-3**. As evident in the 3D data (**Figure 2D** and **Supplementary**
197 **Video 2**), SiR-tubulin staining gathered at spindle poles whilst four axonemes were
198 nucleated and elongated from basal bodies. We quantified the SiR-tubulin staining intensity
199 of microgametocytes for three distinct developmental stages: microgametocytes with a fully
200 formed spindle; newly nucleated axonemes; and developed axonemes (**Figure 2H**). A
201 significant increase in SiR-tubulin staining was quantified across the three stages (**Figure**
202 **2H**), representing the rapid transformation of soluble tubulin into microtubules that occurs
203 during microgametogenesis. This finding was consistent with previous EM studies of
204 microgametogenesis^{15,16}. Notably, we have demonstrated the ability to retrieve and quantify
205 volumetric data from our real-time 4D imaging approach which, prior to this study, has not
206 been possible by EM and limited to fixed samples in immunofluorescence studies.

207 Simultaneously to cytoskeletal rearrangement, microgametocyte morphology was seen to
208 transform from falciform to round, transforming the morphology of the host erythrocyte in the
209 same way (**Figure 2B-CF** and **Supplementary Videos 2-3**). To identify the relationship
210 between rounding up and microtubule polymerisation, we quantified microgametocyte cell
211 circularity and SiR-tubulin staining intensity, respectively. Individual cells were characterised
212 across developmental stages: microgametocytes that were falciform or had a fully developed
213 mitotic spindle, versus those with newly nucleated axonemes or developed axonemes. We
214 found a non-linear relationship between microgametocyte circularity and SiR-tubulin intensity
215 (**Figure 2G**). Individual microgametocytes at the initial developmental stages of
216 microgametogenesis showed varying levels of circularity but a similarly low level of SiR-

217 tubulin intensity. Upon reaching maximal microgametocyte circularity, cells with newly
218 nucleated or developed axonemes showed varying SiR-tubulin intensities, which were at a
219 higher level than the earlier developmental stages. The non-linear relationship between
220 rounding up and microtubule polymerisation revealed that early microtubule polymerisation
221 occurs simultaneously to rounding up and, upon fully rounding up, axonemes continue to
222 elongate and develop (**Figure 2G**)

223

224 **Microgametocyte DNA segregates and localises perpendicularly to spindle poles**

225 Incorporating the DNA dye, Vybrant™ DyeCycle™ Violet, to stain microgametocytes, we
226 next explored the behaviour of the nucleus. Using 3D sectioned data derived from our 4D
227 dataset, we observed nuclear segregation to occur as the microgametocyte genome was
228 replicated (**Figure 2D** and **Supplementary Video 2**). A novel observation was made when
229 comparing the localisation of tubulin and DNA staining, where we observed segregated DNA
230 positioned perpendicularly to basal body tetrads (**Figure 2D**, **Supplementary Video 2** and
231 **Figure 5A**). This showed that the 3D data derived can be used to make novel observations
232 on the biology of microgametocyte DNA replication.

233 Upon full axoneme development, DNA content visibly increased (**Figure 2F**) compared to
234 earlier stages of microgametogenesis (**Figure 2D**). When quantified, a significant increase of
235 DNA staining from spindle formation to nucleation and development of axonemes was found
236 (**Figure 2I**). This demonstrated that the volumetric data can be obtained using our imaging
237 framework, permitting real-time quantification of DNA content and providing a unique window
238 into genome replication.

239

240 **The host erythrocyte perforates and forms a pore for microgametocyte egress**

241 A key stage in microgametogenesis is parasite egress from the host erythrocyte (**Figure 2C**,
242 **E** and **Supplementary Video 3**). 4D imaging revealed that the erythrocyte membrane

243 perforated in preparation for egress (**Figure 2D** and **5A**). Activated microgametocytes
244 aligned at the periphery of the parasite membrane, eventually ejecting from a frequently
245 singular pore that formed in the host erythrocyte (**Figure 2E** and **Supplementary Video 3**).
246 Notably, we observed microgametocytes eject from a spindle pole of the parasite, out of the
247 newly formed host erythrocyte pore (**Figure 2E**, **Figures S1B-D**, **Figure 5A**, and
248 **Supplementary Videos 3,5 and 6**). This finding suggests the mechanism of
249 microgametocyte egress may utilise an unexplored driving force that coordinates ejection
250 from the host cell with spindle pole positioning.

251

252 **Real-time fluorescence imaging of exflagellation**

253 The final steps of microgametogenesis are the emergence of haploid microgametes from the
254 parasite cell body, the remarkably dynamic process of exflagellation. Upon full elongation,
255 the tip of an axoneme aligns at the periphery of the parasite cell body to emerge. When
256 emerging at ~15 minutes post-activation, the developed axoneme carries a haploid genome
257 (1n) from the newly replicated octoploid genome (8n) through the cell surface (**Figure 1A**).
258 Emerging microgametes could be identified either by SiR-tubulin stained axonemes or by the
259 increased motion visible in brightfield, with the latter minimising the effects of phototoxicity.
260 Following the initial emergence of microgametes (**Figure S2** and **Supplementary Video 7**),
261 the full length of axonemes continued to emerge in a rapid motion (**Figure 3**). Full
262 microgamete lengths were visualised by brightfield (**Figure 3A** and **Supplementary Video**
263 **8-9**) and SiR-tubulin (**Figure 3B, C, E** and **Supplementary Videos 10-17**). Host erythrocyte
264 staining during exflagellation revealed the adherence of microgametes to neighbouring
265 erythrocytes (**Figure 3C, E** and **Supplementary Videos 15-17**). DNA staining was notably
266 increased during exflagellation (**Figure 3C, E** and **Supplementary Videos 15-17**) compared
267 to earlier stages of microgametogenesis (**Figure 2B-C** and **3**), signifying successful
268 replication.

269 Due to the dynamic nature of emerging microgametes that were motile through Z-
270 acquisition, 2D rather than 3D time-lapse data was acquired during exflagellation. Although
271 3D frames of exflagellation were not obtained, it is possible to obtain 3D plots of SiR-tubulin
272 intensity staining (**Figure 3D**). This allowed the identification of dense regions of SiR-tubulin
273 staining resulting from axoneme overlap, which would otherwise not be deducible without 4D
274 imaging (**Figure 3D**). Alternatively, as parasite motion halts during loss of viability, 3D data
275 can be obtained to closely observe the positioning of emerged microgametes (**Figure 3E**
276 and **Supplementary Video 17**), demonstrating about ability to acquire both 2D and 3D
277 exflagellation time-lapse data.

278

279 **Drug inhibition of microgametogenesis**

280 The process of microgametogenesis is tightly synchronised by a series of cell cycle
281 regulators and is consequently sensitive to and the target of known and developmental drug
282 treatments²⁵. We sought to apply our 4D imaging approach as a drug discovery tool that
283 could help elucidate the cellular phenotypes of compounds with known and unknown activity
284 against microgametogenesis regulators towards defining their mode or process of action.

285 Compounds 1294^{31,34} and ML10³⁵ have been well-established as potent inhibitors of
286 microgametogenesis regulators Ca²⁺-dependent protein kinase 4 (CDPK4) and cyclic-GMP
287 dependent protein kinase G (PKG), respectively. CDPK4 tightly regulates three processes
288 during microgametogenesis: initiation of the first genome replication, mitotic spindle
289 assembly and microgamete motility³¹. PKG has roles in the regulation of Ca²⁺ levels and
290 rounding up during gametogenesis^{36,37}. The cellular phenotype of 1294^{31,34} and ML10³⁵ have
291 been previously reported using immunofluorescence staining of fixed microgametocytes³⁸.
292 Using 4D imaging, we could resolve distinct cellular phenotypes for each drug and its target
293 (**Figure 4A-B, D-H** and **Supplementary Videos 18-24**).

294 CDPK4 inhibition by 1294^{31,34} prevented morphological transformation from falciform to
295 round (**Figure 4A** and **G**), DNA replication (**Figure 4F**) and microtubule polymerisation

296 (Figure 4D-E) during microgametogenesis (Supplementary Videos 18-22). On detailed
297 inspection, 1294-treated parasites, failed to reach the maximum level of cell circularity
298 (Figure 4G) and SiR-tubulin intensity (Figure 4A, D, E and G), indicating a role of CDPK4 in
299 microgametocyte rounding as well as cytoskeletal rearrangement during
300 microgametogenesis. Of note, many 1294-treated microgametocytes were observed to have
301 egressed from the onset of activation, a probable stress-response of CDPK4 inhibition
302 (Figure 4A). Of the population of 1294-treated microgametocytes, 50% were able to fully
303 egress compared to the 53% of untreated microgametocytes which egressed from the host
304 erythrocyte (Figure 4H). An incomplete egress phenotype in which falciform parasites
305 partially emerged from the host erythrocyte was also observed, with 15% of 1294-treated
306 parasites demonstrating this phenotype (Figure 4H). 3D data revealed the positioning of the
307 MTOC which failed to transform to eight basal bodies (Figure 4A and Supplementary
308 Video 19). This suggests that CDPK4 plays an early role in DNA replication, microtubule
309 polymerisation, rounding up and host erythrocyte egress during microgametogenesis. This
310 phenotype is consistent with published findings on 1294-treatment of *P. falciparum*³⁸ and *P.*
311 *berghei*³¹ gametocytes, with the exception that our morphological rounding phenotype is not
312 observed in *P. berghei* gametocytes which are already round prior to activation. The
313 deduced overall cellular phenotype of CDPK4 inhibition is summarised in Figure 5B.
314 PKG inhibition by ML10³⁵ was observed next, clearly demonstrating arrest of
315 microgametocytes before cell-rounding (Figure 4B and G and Supplementary Videos 23-
316 24), replication of DNA (Figure 4F) and microtubule polymerisation (Figure 4D and E).
317 ML10-treated gametocytes retained a falciform morphology and a level of SiR-tubulin
318 staining on par with that seen at the onset of gametogenesis activation (Figure 4D-E and G
319 and Supplementary Videos 23-24). SiR-tubulin intensity was significantly lower than
320 untreated microgametocytes at 10 minutes post-activation (Figure 4E). The host erythrocyte
321 egress phenotype was mixed, as 50% of ML10-treated cells emerged fully, 50% failed
322 (Figure 4Bii) and 8% partially emerged (Figure 4Bi) from the host erythrocyte (Figure 4A,

323 **H** and **Supplementary Videos 23-24**). We can deduct from these images that PKG plays a
324 significant role in regulating MTOC transformation, axoneme nucleation and elongation, DNA
325 replication and rounding up exhibited in microgametogenesis, as summarised in **Figure 5C**.
326 These observations match previously reported studies on PKG during
327 microgametogenesis^{38,39} and does so without the laborious staining steps of fixed parasite
328 imaging.

329

330 **The microgametocyte proteasome plays a crucial role in microgametogenesis**

331 To extend the cellular dissection of microgametogenesis, we next sought to test the role of
332 the proteasome in cellular reorganisation of the microgametocyte using the drug bortezomib,
333 a proteasome-inhibitor that has not been explored during microgametogenesis. Bortezomib
334 is active against the asexual blood stages of *Plasmodium*⁴⁰ and the eukaryote and
335 euryarchaeota proteasomes⁴¹⁻⁴³. A recent study on the 20S proteasome of *S. acidocaldarius*
336 reported bortezomib arrested cells in the midst of division⁴⁴. Given the role of the
337 proteasome in *S. acidocaldarius* cell division and interest in its use as an antimalarial drug
338 target⁴⁵ we aimed to deduce the role of the proteasome in regulation of microgametogenesis
339 DNA replication and cytoskeletal rearrangement.

340 Proteasome inhibition by bortezomib resulted in a block of microgametogenesis, preventing
341 full cytoskeletal rearrangement (**Figure 4D, E and G**), DNA replication (**Figure 4F**) and
342 exflagellation (**Figure 4C**). Most cells were also shown to fail to egress from the host
343 erythrocyte, although this phenotype was mixed (**Figure 4H**). We observed inhibition of the
344 *P. falciparum* proteasome impacted the transformation of the microgametocyte MTOC,
345 visible as 2 small nodes of SiR-tubulin staining which remained at one pole of the parasite
346 (**Figure 4Ci** and **Supplementary Videos 25**). The transformed MTOC was subsequently
347 able to nucleate axonemes from one end of the parasite, but no more than 3 axonemes were
348 formed and growth was truncated (**Figure 4Cii-iii** and **Supplementary Videos 25-28**). This
349 perturbation to axoneme nucleation and elongation resulted in a significant decrease in SiR-

350 tubulin staining intensity (**Figure 4D, E and G**), although less significant than the decrease
351 observed with ML10 and 1294 treatment which blocked all microtubule polymerisation.
352 Proteasome-inhibited microgametocytes were, however, able to transform from falciform to
353 round (**Figure 4G** and **Supplementary Videos 25-28**).
354 Bortezomib treatment also significantly reduced Vybrant™ DyeCycle™ Violet staining
355 intensity, signifying a probable indirect inhibitory effect on DNA replication (**Figure 4F**).
356 Additionally, we observed incomplete transformation of the MTOC which resulted in
357 truncated formation of few axonemes from one pole of developing microgametocytes.
358 Combined these data represent the first time that the cellular role of the proteasome during
359 microgametogenesis has been explored. Our findings, summarised in **Figure 5C**, add further
360 weight to bortezomib's use as a desirable antimalarial drug candidate that is able to inhibit
361 the sexual stages of *Plasmodium* in addition to asexual replication, representing the
362 potential to treat symptoms and block transmission with a single compound.

363 **DISCUSSION**

364 To date, detailed observation of *P. falciparum* microgametogenesis has mostly centred
365 around fixed parasite imaging, with studies utilising immunofluorescence labelling²⁵ or
366 electron microscopy¹⁴⁻¹⁶. Although these studies have been pivotal in developing our current
367 understanding of microgametogenesis cell biology, imaging fixed parasites is limited by the
368 extensive sample preparation steps and fails to resolve the dynamic nature of underlying
369 cellular events. Here, we have developed a live-cell 3D fluorescence imaging approach (4D
370 imaging) that captures the dynamics of *P. falciparum* microgametogenesis from activation to
371 exflagellation in fine detail. Utilising widefield microscopy, commercially available stains, *in*
372 *vitro* *P. falciparum* culture and an open-source software for analysis we present a
373 methodological approach that will be readily utilisable for other research groups.

374 Using a combination of a cell-permeable fluorogenic probe, DNA dye and lectin we can label
375 and observe development of microgametocyte microtubules, DNA and the host erythrocyte
376 membrane, respectively. Whilst live fluorescence imaging is often impeded by phototoxicity,
377 here we have devised a method that maximises the length of time-lapse image acquisition
378 without compromising microgametocyte viability. Our approach permits the acquisition of
379 microgametogenesis in full over two stages: early and late development, capturing spindle
380 formation through to full axoneme development and exflagellation, respectively. Importantly,
381 our imaging approach permits volumetric quantification of 3D data through time which we
382 demonstrate as a powerful tool in defining drug phenotypes. Our approach is consequently
383 applicable to future comparative studies of alternative drug treatment and *P. falciparum*
384 transgenic cell lines to wild-type phenotypes.

385 In line with previous studies on microgametogenesis^{13,16}, we observed the rapid production
386 of basal bodies from a single MTOC to initiate nucleation and elongation of axonemes,
387 simultaneously to DNA replication and egress. Coupling live fluorescence microscopy to
388 fluorescence intensity and 3D analyses, we observed nuclei to segregate and align
389 perpendicularly to basal bodies in the early stages of microgametogenesis. Whilst

390 synchronous segregation of developing microgametocyte genomes and basal bodies has
391 been reported¹³, live fluorescence imaging provides novel insight into the positioning of the
392 newly replicated DNA. Furthermore, we find egress involves perforation and pore formation
393 of the host erythrocyte membrane. Previous studies have reported swelling of the host
394 erythrocyte prior to PVM rupture and vesiculation during *P. berghei* microgametogenesis⁷.
395 Here, upon erythrocyte pore formation we observed egress of developing *P. falciparum*
396 microgametocytes to occur from a spindle pole of the microgametocyte. This suggests that
397 there may be forces occurring from a single pole of the microgametocyte that drive egress
398 from the host erythrocyte. Future investigation of pore-forming proteins and their role in this
399 process may also be of relevance.

400 Additionally, we demonstrate the applicability of our workflow to the study of transmission
401 blocking drug phenotypes. We have used the live imaging framework to elucidate the cellular
402 phenotypes of 1294 and ML10, known inhibitors of microgametogenesis regulators CDPK4
403 and PKG, respectively. We have also defined the proteasome as a crucial component of
404 microgametogenesis regulation and for the first time, we define bortezomib as a powerful
405 inhibitor of *P. falciparum* transmission. This finding points to the importance of the
406 degradation of misfolded proteins and regulation of functional protein abundance in
407 permitting transmission of the *Plasmodium* microgametocytes. Our approach generates
408 reproducible and consistent phenotypes to fixed parasite studies whilst, critically, not
409 requiring complex fixation or staining steps.

410 As drug and insecticide resistance has threatened existing antimalarial treatment strategies,
411 there is an urgent need for novel transmission-blocking antimalarials that can be used
412 singularly or in combination with schizonticides, killing asexual stages. Developing a full
413 understanding of the mode of action of antimalarial drug candidates maximises the likelihood
414 of clinical safety and future administration. Our imaging approach permits deeper
415 understanding of this remarkable cell biology process, capturing real-time development with
416 fluorescence which may otherwise be missed with fixed or brightfield imaging. The data

417 depicted here promises to unveil novel insights into *P. falciparum* microgametogenesis for
418 cell biology and drug study, but the protocol is not limited to this. Cultivation of *in vitro*
419 *Plasmodium* cultures, at any stage, permits the live microscopy of the breadth of malaria
420 parasite development, from macrogametogenesis and asexual blood stage development to
421 liver stages. Additional stains for intracellular organelles, parasite membranes and sex-
422 specific proteins, with both wild-type and transgenic lines, will now be a priority for exploring
423 so that we can shed further light on this ancient but deadly single-celled parasite.

424 **MATERIALS AND METHODS**

425 ***In vitro culture of Plasmodium falciparum***

426 *P. falciparum* NF54 strain parasites were cultured as previously described³³. Asexual
427 parasite cultures were maintained between 0.75-5% parasitaemia and 4% haematocrit using
428 human erythrocytes (NHS National Blood Service). Erythrocytes were supplemented with 3
429 units/ml heparin (Sigma-Aldrich). Parasites were grown in asexual parasite culture medium
430 (RPMI 1640 with 25 mM HEPES (Life Technologies) supplemented with 50 µg/ml
431 hypoxanthine (Sigma), 0.3 g/l L-glutamine (Sigma) and 10% human serum (Interstate Blood-
432 Bank)). Gametocyte cultures were induced from asexual parasite cultures at 3% asexual
433 parasitaemia and 4% haematocrit. Gametocyte culture media (RPMI 1640 with 25 mM
434 HEPES supplemented with 150 µg/ml L-glutamine, 2.78 mg/ml sodium bicarbonate, 2 mg/ml
435 D-glucose, 50 µg/ml hypoxanthine, 5% human serum and 5% AlbuMAX-II (Gibco)) was
436 replaced daily until reaching maturity at day 14-post induction. All cultures were maintained
437 at 37°C under 3% O₂/5% CO₂/93% N₂ (BOC, UK).

438 Upon reaching maturity, gametocyte viability was determined by measuring the rate of
439 exflagellation relative to erythrocyte density. Gametocyte culture was treated with ookinete
440 media (RPMI 1640 supplemented with 2 g/l sodium bicarbonate, 50 mg/l hypoxanthine and
441 100 mM xantharic acid (XA) (Sigma-Aldrich), pH adjusted to 7.4) to activate
442 gametogenesis. Exflagellation events and erythrocyte density was counted using a
443 haemocytometer (VWR) and Nikon Leica DC500 microscope.

444 ***Staining and Treating Live P. falciparum Gametocytes***

445 For live-cell fluorescence imaging, samples of mature gametocyte culture (> 0.3%
446 exflagellation) were stained with 500 nM SiR-tubulin (Spirochrome) for 3 hours at 37°C.
447 Samples were additionally stained with 5 µg/ml wheat germ agglutinin (WGA) conjugated to
448 AlexaFluor488 (Invitrogen) and 500 nM Vybrant™ DyeCycle™ Violet for 30 minutes at 37°C.

449 Stained samples were protected from light and strictly maintained at 37°C, to prevent
450 premature activation, until imaging.

451 Samples were treated with 10 µM 1294⁴⁶, 10 µM ML10³⁵, 25 µM Bortezomib or DMSO and
452 normalised to 0.25% DMSO for 3 hours at 37°C, before imaging.

453 ***Imaging Live Microgametogenesis by Widefield Microscopy***

454 Wells of an Ibidi 8-well µ-Slide were pre-treated with 140 µl ookinete medium and slides
455 were pre-positioned on the microscope stage. To activate gametogenesis, 6 µL of the
456 stained gametocytes, equating to ~30 million total erythrocytes, was added directly to
457 ookinete media-treated wells at room temperature (21°C). Samples were imaged with a
458 Prime 95B sCMOS camera (photometrics) on a Nikon Ti2-E widefield microscope using x
459 100 Plan Apo 1.4 numerical aperture (NA) oil objective with NIS Elements v4.20 software.
460 SiR-Tubulin, WGA-488 and Vybrant™ DyeCycle™ Violet staining were imaged with a Cy5,
461 GFP and DAPI filter set. The triggered multi-wavelength LED and static quad band filter
462 cube was used in acquisition through Z and between wavelengths.

463 Early stages of microgametogenesis (0-10 minutes) were acquired as 3D datasets through
464 time at 'no delay' and with 34 ms exposure time. Z-stacks were acquired at 0.2 µm steps
465 from above and below the cell with a Piezo driven stage. Acquisition was alternated between
466 brightfield and fluorescence to minimise phototoxicity and subsequently prolong parasite
467 viability. Exflagellation was captured as 2D (single z-slice) datasets, acquiring with no delay
468 between frames.

469 ***Image Analysis***

470 The open-source bioimage analysis software Icy⁴⁷ was used to analyse all time-lapse
471 datasets. All 3D datasets are depicted here as 2D maximum intensity projections. Early
472 developmental stages of microgametogenesis, acquired through t and z, were deconvolved
473 using a custom-made Protocol in Icy. The Protocol is attached in the **Additional**
474 **Supplementary Information**. Within the Protocol, a Sequence File Batch loop locates the

475 3D+t files from which a channel of interest is extracted. The selected channel of each time
476 frame is processed as an individual 3D stack. The metadata of each stack is read and used
477 as an input for the EpiDEMIC deconvolution bloc (Epifluorescence Deconvolution
478 MIcroscopy), a blind (i.e. without Point Spread Function (PSF) knowledge) deconvolution
479 method for widefield fluorescence microscopy 3D data⁴⁸. All timelapses were deconvolved
480 over 50 iterations and 2 loops.

481 All 2D timelapse data and 3D data depicted as 2D maximum intensity projections or 3D
482 sectioned views were created using Icy. To quantify SiR-tubulin and Vybrant™ DyeCycle™
483 Violet intensity, egress phenotypes and cell circularity, raw 3D data was converted to 2D
484 maximum intensity projections in NIS Elements v4.20 prior to analysis. Egress phenotypes
485 were quantified by manual observation. To measure the circularity and staining intensity of
486 individual cells, each cell was defined as a custom region of interest. The SiR-tubulin and
487 Vybrant™ DyeCycle™ Violet staining intensity of each individual cell was quantified using
488 the time-measurement function in NIS Elements v4.20 and is reported in arbitrary units. The
489 circularity of each cell was measured using the Automated Measurement feature in NIS
490 Elements v4.20. Circularity is reported here as shape measure values from 0-1 derived from
491 the area and perimeter of each cell, with higher values representing shapes of increasing
492 circularity and circles being characterised as a value of 1. All graphical and statistical data
493 was analysed with GraphPad Prism version 8.0.

494 **REFERENCES**

- 495 1. Josling, G.A. & Llinás, M. Sexual development in *Plasmodium* parasites: knowing
496 when it's time to commit. *Nat Rev Microbiol* **13**, 573-87 (2015).
- 497 2. Dixon, M.W., Dearnley, M.K., Hanssen, E., Gilberger, T. & Tilley, L. Shape-shifting
498 gametocytes: how and why does *P. falciparum* go banana-shaped? *Trends Parasitol*
499 **28**, 471-8 (2012).
- 500 3. Dixon, M.W.A. & Tilley, L. *Plasmodium falciparum* goes bananas for sex. *Mol
501 Biochem Parasitol* **244**, 111385 (2021).
- 502 4. Billker, O., Shaw, M.K., Margos, G. & Sinden, R.E. The roles of temperature, pH and
503 mosquito factors as triggers of male and female gametogenesis of *Plasmodium*
504 *berghei* in vitro. *Parasitology* **115** (Pt 1), 1-7 (1997).
- 505 5. Andreadaki, M. et al. Sequential Membrane Rupture and Vesiculation during
506 *Plasmodium berghei* Gametocyte Egress from the Red Blood Cell. *Scientific Reports*
507 **8**, 3543 (2018).
- 508 6. Guttery, D.S., Roques, M., Holder, A.A. & Tewari, R. Commit and Transmit:
509 Molecular Players in *Plasmodium* Sexual Development and Zygote Differentiation.
510 *Trends in Parasitology* **31**, 676-685 (2015).
- 511 7. Andreadaki, M. et al. Sequential Membrane Rupture and Vesiculation during
512 *Plasmodium berghei* Gametocyte Egress from the Red Blood Cell. *Sci Rep* **8**, 3543
513 (2018).
- 514 8. Ponzi, M. et al. Egress of *Plasmodium berghei* gametes from their host erythrocyte is
515 mediated by the MDV-1/PEG3 protein. *Cell Microbiol* **11**, 1272-88 (2009).
- 516 9. Talman, A.M. et al. PbGEST mediates malaria transmission to both mosquito and
517 vertebrate host. *Mol Microbiol* **82**, 462-74 (2011).
- 518 10. Deligianni, E. et al. Critical role for a stage-specific actin in male exflagellation of the
519 malaria parasite. *Cell Microbiol* **13**, 1714-30 (2011).
- 520 11. Deligianni, E. et al. A perforin-like protein mediates disruption of the erythrocyte
521 membrane during egress of *Plasmodium berghei* male gametocytes. *Cell Microbiol*
522 **15**, 1438-55 (2013).
- 523 12. Olivieri, A. et al. Distinct properties of the egress-related osmiophilic bodies in male
524 and female gametocytes of the rodent malaria parasite *Plasmodium berghei*. *Cell
525 Microbiol* **17**, 355-68 (2015).
- 526 13. Sinden, R.E., Canning, E.U., Bray, R.S. & Smalley, M.E. Gametocyte and gamete
527 development in *Plasmodium falciparum*. *Proc R Soc Lond B Biol Sci* **201**, 375-99
528 (1978).
- 529 14. Billker, O. et al. Azadirachtin disrupts formation of organised microtubule arrays
530 during microgametogenesis of *Plasmodium berghei*. *J Eukaryot Microbiol* **49**, 489-97
531 (2002).
- 532 15. Sinden, R.E., Canning, E.U. & Spain, B. Gametogenesis and fertilization in
533 *Plasmodium yoelii nigeriensis*: a transmission electron microscope study. *Proc R Soc
534 Lond B Biol Sci* **193**, 55-76 (1976).
- 535 16. Sinden, R.E., Talman, A., Marques, S.R., Wass, M.N. & Sternberg, M.J. The
536 flagellum in malarial parasites. *Curr Opin Microbiol* **13**, 491-500 (2010).
- 537 17. Sinden, R.E. Malaria, sexual development and transmission: retrospect and
538 prospect. *Parasitology* **136**, 1427-34 (2009).
- 539 18. Bell, A. Microtubule Inhibitors as Potential Antimalarial Agents. *Parasitology Today*
540 **14**, 234-240 (1998).
- 541 19. Rawlings, D.J. et al. α -Tubulin II is a male-specific protein in *Plasmodium falciparum*.
542 *Molecular and Biochemical Parasitology* **56**, 239-250 (1992).
- 543 20. Angrisano, F., Tan, Y.H., Sturm, A., McFadden, G.I. & Baum, J. Malaria parasite
544 colonisation of the mosquito midgut--placing the *Plasmodium* ookinete centre stage.
545 *Int J Parasitol* **42**, 519-27 (2012).

546 21. Ruecker, A. et al. A male and female gametocyte functional viability assay to identify
547 biologically relevant malaria transmission-blocking drugs. *Antimicrob Agents
548 Chemother* **58**, 7292-302 (2014).

549 22. Bertiaux, E. et al. Expansion microscopy provides new insights into the cytoskeleton
550 of malaria parasites including the conservation of a conoid. *PLoS Biol* **19**, e3001020
551 (2021).

552 23. Sinden, R.E. Gametocytogenesis of *Plasmodium falciparum* in vitro: an electron
553 microscopic study. *Parasitology* **84**, 1-11 (1982).

554 24. Ashdown, G.W. et al. A machine learning approach to define antimalarial drug action
555 from heterogeneous cell-based screens. *bioRxiv* (2019).

556 25. Delves, M.J. et al. A high throughput screen for next-generation leads targeting
557 malaria parasite transmission. *Nat Commun* **9**, 3805 (2018).

558 26. Geoghegan, N.D. et al. 4D analysis of malaria parasite invasion offers insights into
559 erythrocyte membrane remodeling and parasitophorous vacuole formation. *Nature
560 Communications* **12**, 3620 (2021).

561 27. Zeeshan, M. et al. Protein phosphatase 1 regulates atypical mitotic and meiotic
562 division in *Plasmodium* sexual stages. *Communications Biology* **4**, 760 (2021).

563 28. Wall, R.J. et al. *Plasmodium* APC3 mediates chromosome condensation and
564 cytokinesis during atypical mitosis in male gametogenesis. *Sci Rep* **8**, 5610 (2018).

565 29. Lukinavičius, G. et al. Fluorogenic probes for live-cell imaging of the cytoskeleton.
566 *Nature Methods* **11**, 731-733 (2014).

567 30. Dubois, J. et al. Fluorescent and biotinylated analogues of docetaxel: Synthesis and
568 biological evaluation. *Bioorganic & Medicinal Chemistry* **3**, 1357-1368 (1995).

569 31. Fang, H. et al. Multiple short windows of calcium-dependent protein kinase 4 activity
570 coordinate distinct cell cycle events during *Plasmodium* gametogenesis. *eLife* **6**,
571 e26524 (2017).

572 32. Hitz, E., Balestra, A.C., Brochet, M. & Voss, T.S. PfMAP-2 is essential for male
573 gametogenesis in the malaria parasite *Plasmodium falciparum*. *Scientific Reports* **10**,
574 11930 (2020).

575 33. Delves, M.J. et al. Routine in vitro culture of *P. falciparum* gametocytes to evaluate
576 novel transmission-blocking interventions. *Nat Protoc* **11**, 1668-80 (2016).

577 34. Doggett, J.S., Ojo, K.K., Fan, E., Maly, D.J. & Van Voorhis, W.C. Bumped kinase
578 inhibitor 1294 treats established *Toxoplasma gondii* infection. *Antimicrob Agents
579 Chemother* **58**, 3547-9 (2014).

580 35. Baker, D.A. et al. A potent series targeting the malarial cGMP-dependent protein
581 kinase clears infection and blocks transmission. *Nat Commun* **8**, 430 (2017).

582 36. McRobert, L. et al. Gametogenesis in Malaria Parasites Is Mediated by the cGMP-
583 Dependent Protein Kinase. *PLOS Biology* **6**, e139 (2008).

584 37. Bennink, S., Kiesow, M.J. & Pradel, G. The development of malaria parasites in the
585 mosquito midgut. *Cellular Microbiology* **18**, 905-918 (2016).

586 38. Yahya, S. et al. *Plasmodium falciparum* protein Pfs16 is a target for transmission-
587 blocking antimalarial drug development. *bioRxiv*, 2021.06.14.448287 (2021).

588 39. McRobert, L. et al. Gametogenesis in malaria parasites is mediated by the cGMP-
589 dependent protein kinase. *PLoS Biol* **6**, e139 (2008).

590 40. Reynolds, J.M., El Bissati, K., Brandenburg, J., Günzl, A. & Mamoun, C.B.
591 Antimalarial activity of the anticancer and proteasome inhibitor bortezomib and its
592 analog ZL3B. *BMC clinical pharmacology* **7**, 13-13 (2007).

593 41. Adams, J. et al. Proteasome Inhibitors: A Novel Class of Potent and Effective
594 Antitumor Agents. *Cancer Research* **59**, 2615-2622 (1999).

595 42. Chen, D., Frezza, M., Schmitt, S., Kanwar, J. & Dou, Q.P. Bortezomib as the first
596 proteasome inhibitor anticancer drug: current status and future perspectives. *Curr
597 Cancer Drug Targets* **11**, 239-53 (2011).

598 43. Fu, X. et al. Ubiquitin-Like Proteasome System Represents a Eukaryotic-Like
599 Pathway for Targeted Proteolysis in Archaea. *mBio* **7**(2016).

600 44. Tarrason Risa, G. et al. The proteasome controls ESCRT-III-mediated cell division in
601 an archaeon. *Science* **369**, eaaz2532 (2020).

602 45. Xie, S.C. et al. Target Validation and Identification of Novel Boronate Inhibitors of the
603 Plasmodium falciparum Proteasome. *J Med Chem* **61**, 10053-10066 (2018).

604 46. Ojo, K.K. et al. A specific inhibitor of PfCDPK4 blocks malaria transmission:
605 chemical-genetic validation. *J Infect Dis* **209**, 275-84 (2014).

606 47. de Chaumont, F. et al. Icy: an open bioimage informatics platform for extended
607 reproducible research. *Nat Methods* **9**, 690-6 (2012).

608 48. Soulez, F., Denis, L., Tourneur, Y. & Thiébaut, É. Blind deconvolution of 3D data in
609 wide field fluorescence microscopy. in *International Symposium on Biomedical*
610 *Imaging* CDROM (2012).

611

612 **ACKNOWLEDGEMENTS**

613 We thank Irene Garcia-Barbazan, Eliana Real and David Grimson for assisting with parasite
614 culture and for sharing expert transmission advice. Additional thanks to other members of
615 the Baum lab for helpful discussions and experimental support, with particular thanks to
616 Thomas C. A. Blake for assistance in data production. We also thank Robert E. Sinden for
617 valuable discussions about the biology of microgametogenesis. Finally, we thank
618 collaborators in the Baker lab and Van Voorhis lab for their generous donation of
619 microgametogenesis inhibitors 1294 and ML10, respectively.

620

621 **AUTHOR CONTRIBUTIONS**

622 S.Y., S.J., G.A. and J.B. designed experiments. S.Y., S.J., H.S., D.G. and G.A. performed
623 and analysed experiments. S.Y., S.J., M.T.F, A.C, F.D and E.R. cultured *P. falciparum*.
624 D.C.A.G designed the Icy batch deconvolution protocol.

625

626 **COMPETING INTERESTS**

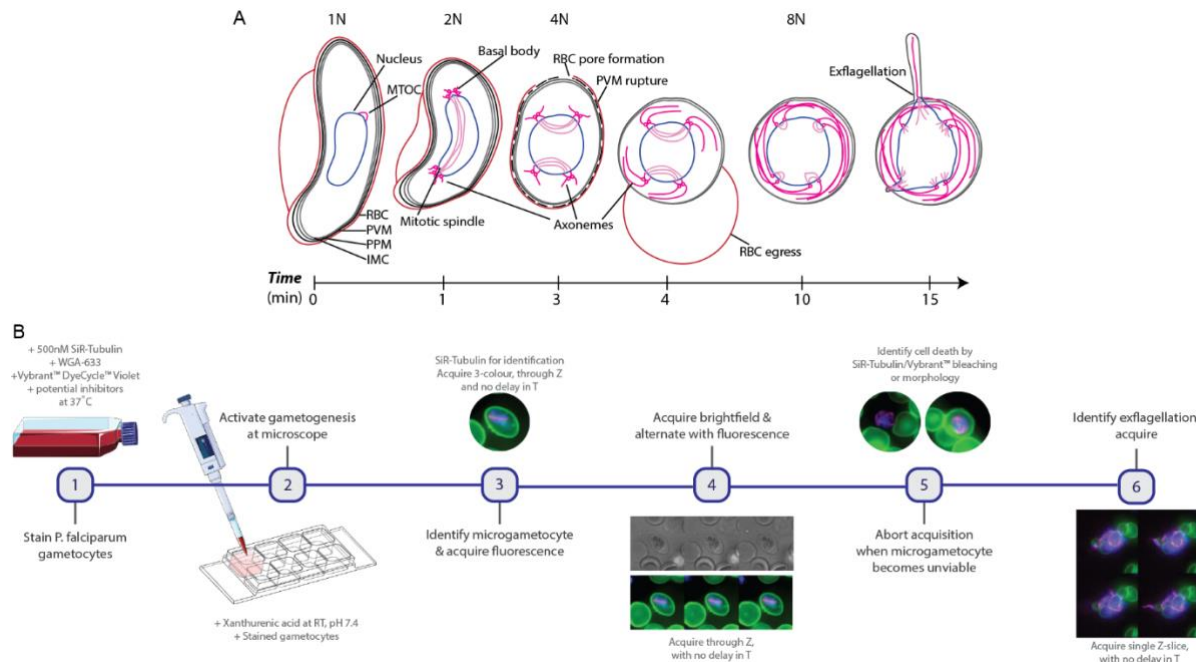
627 The authors declare no competing interests.

628

629 **FUNDING**

630 S.Y. is supported by a Ph.D. studentship from an EPSRC Doctoral Training Partnership
631 award (Grant EP/R512540/1) to Imperial College London. JB was supported by an
632 Investigator Award from Wellcome (100993/Z/13/Z). This work was funded in part by an
633 award to JB from the Bill and Melinda Gates Foundation (OPP1181199). The Facility for
634 Imaging by Light Microscopy (FILM) at Imperial College London is part-supported by funding
635 from the Wellcome Trust (grant 104931/Z/14/Z) and BBSRC (grant BB/L015129/1)

636 **FIGURES**

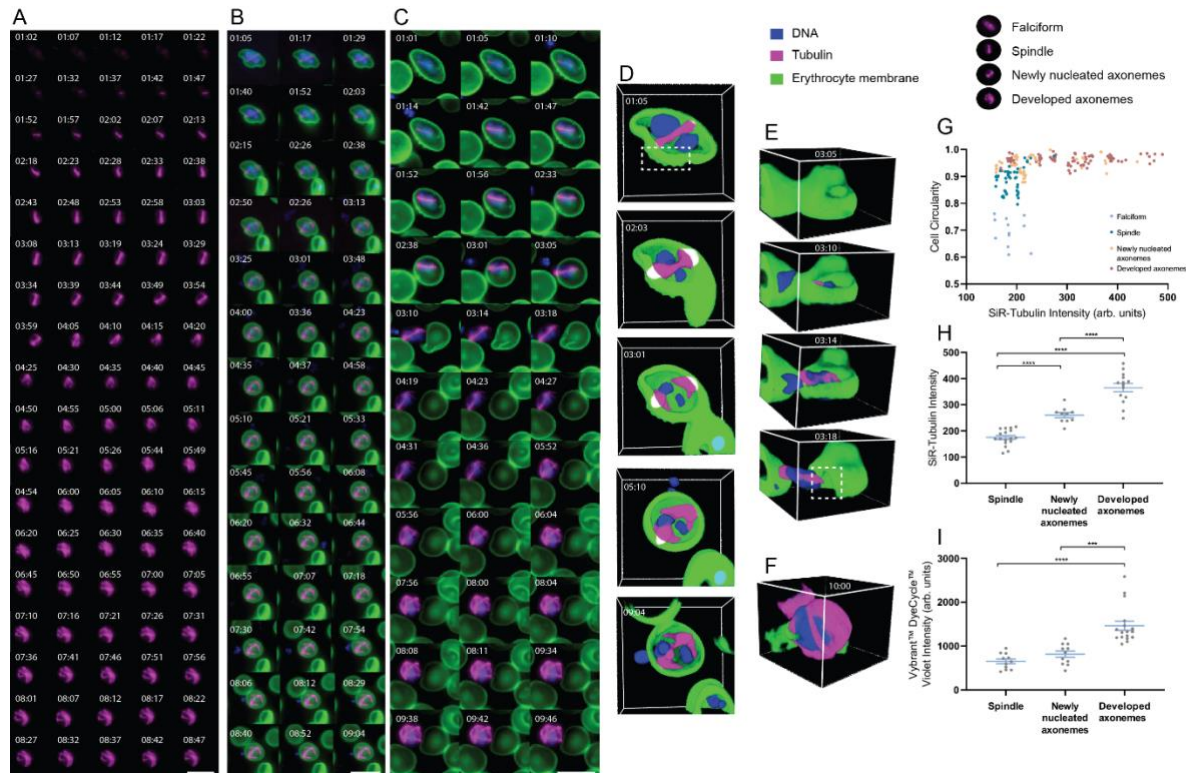


637

638 **Figure 1. *P. falciparum* microgametogenesis and our live cell imaging approach**

639 **(A)** Details of the cell biological transformations occurring during microgametogenesis from
640 activation at $t = 0$ minutes to exflagellation at $t = 15$ minutes. At $t = 0$ minutes,
641 microgametocytes start with a falciform morphology and an in-tact 4-layer membrane,
642 comprised of the red blood cell (RBC) membrane, parasitophorous vacuole membrane
643 (PVM), parasitophorous plasma membrane (PPM) and inner membrane complex (IMC).
644 Following the first round of DNA replication (1n-2n) at $t = 1$ minute, the microtubule
645 organising centre (MTOC) transforms to two tetrads of basal bodies joined by a mitotic
646 spindle. Further replication of DNA (2n-4n, 4n-8n) occurs after $\sim t = 3-4$ minutes,
647 simultaneously to the separation of basal bodies and egress. During egress, PVM rupture
648 precedes erythrocyte egress (inside-out-mechanism) and parasites egress from an
649 erythrocyte pore. Axonemes nucleate from basal bodies following the first DNA replication at
650 $t = 1$ min and elongate from $t = 1-15$ min, coiling around the parasite cell body. At 15 minutes
651 post-activation, axonemes emerge attached to a haploid genome as microgametes, in the
652 process of exflagellation. **(B)** The workflow of live gametocyte staining and fluorescence
653 microscopy of microgametogenesis. *P. falciparum* NF54 gametocytes are stained with SiR-
654 Tubulin, WGA-633 and Vybrant™ DyeCycle™ Violet at 37°C, at which point inhibitors of
655 microgametogenesis may be added. Stained gametocytes are subsequently activated with
656 ookinete medium in pre-positioned imaging slides at RT. SiR-tubulin stained mitotic spindles
657 are used to identify microgametogenesis events, which are continually imaged through T
658 and Z, alternating between brightfield and fluorescence to minimise phototoxicity. When

659 parasites are deemed unviable based on photobleaching or morphology, exflagellation
660 events are captured as single Z-slice timelapses through T.



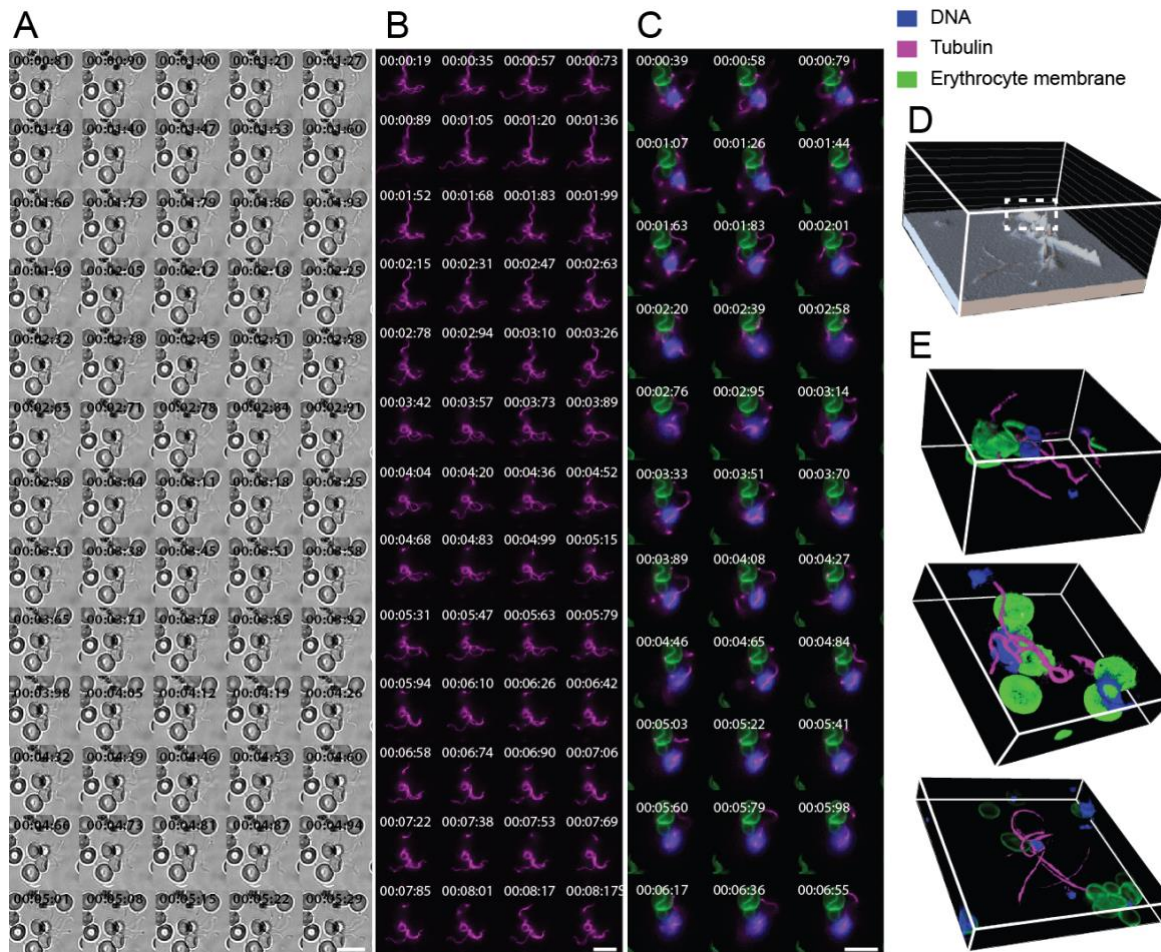
661

662 **Figure 2. Tubulin dynamics, egress and DNA replication during *P. falciparum***
663 **microgametogenesis**

664 Still timelapses of microgametocytes stained with (A) SiR-Tubulin (magenta) only and (B-E)
665 a combination of SiR-Tubulin (magenta), WGA-488 (green) and Vybrant™ DyeCycle™
666 Violet (blue) in the early developmental stages of microgametogenesis. See **Supplementary**
667 **Videos 1, 2 and 3** for corresponding timelapses of A-C. Microtubule staining (magenta)
668 portrays formation of mitotic spindles, basal bodies and axonemes. (B-E) Timelapse data
669 depicting DNA replication (blue), microtubule dynamics (magenta), host erythrocyte egress
670 and morphological transformations (host erythrocyte membrane, green). (D) Erythrocyte
671 membrane perforation (white dashed box), (E) erythrocyte pore formation (white dashed
672 box) and (F) axoneme coiling are visible in 3D sectioned images. (G) A graph plotted to
673 show cell circularity and SiR-Tubulin intensity (arbitrary units), with each plot representing
674 individual cells of a given developmental stage; falciform ($n = 12$), spindle ($n = 46$), newly
675 nucleated axonemes ($n = 48$) and developed axonemes ($n = 82$). Representative images of
676 developmental stages are above the plots. (H) SiR-Tubulin intensity (arbitrary units) of
677 individual cells from distinct developmental stages; spindle ($n = 17$), newly nucleated
678 axonemes ($n = 10$) and developed axonemes ($n = 14$). (I) Vybrant™ DyeCycle™ Violet
679 intensity (arbitrary units) quantified in distinct developmental stages; spindle ($n = 11$), newly
680 nucleated axonemes ($n = 11$) and developed axonemes ($n = 17$). Significant differences in
681 stain intensities between developmental stages was calculated with an unpaired, two-tailed t

682 test (*** $p < .001$, **** $p < .0001$). **A-C** 2D maximum intensity projection of 3D data, scale
683 bars = 10 μm . Individual channels of **B** and **C** can be found in **Figure S1A** and **Figure S1B**,
684 respectively. **D-E** 3D sectioned views frames depicted in **B-C**, respectively. **A-E** Time is
685 depicted as minutes and seconds (mm:ss). All imaging data depicted reflect observations
686 from >10 biological replicates.

687

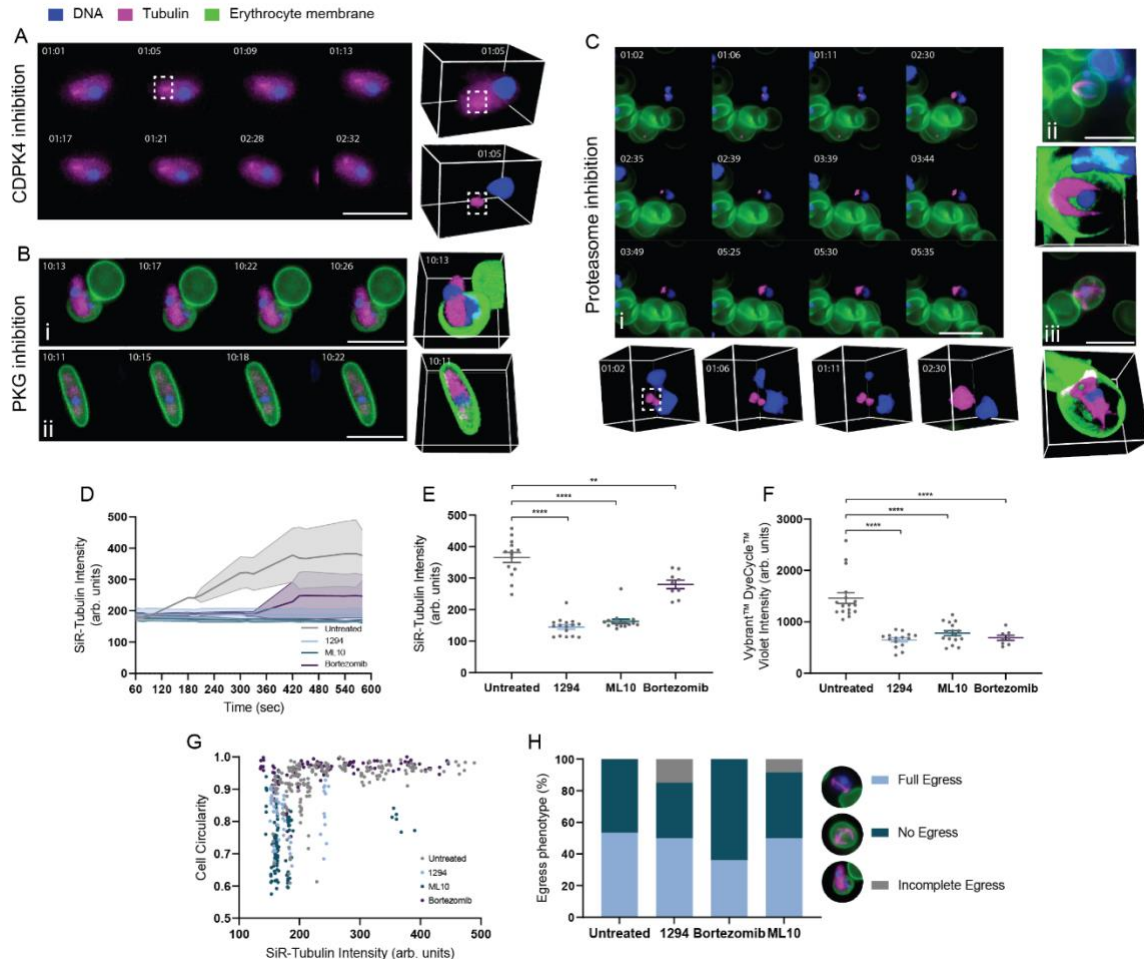


688

689 **Figure 3. Exflagellation of *P. falciparum* microgametes**

690 2D timelapse stills of exflagellation imaged by (A) brightfield and (B, C & E) fluorescence
691 microscopy. See **Supplementary Videos 8, 10 and 15** for corresponding timelapses of A-C.
692 (B-C) SiR-Tubulin-stained axonemes (magenta) emerge from the parasite cell as
693 microgametes. (C) Emerging microgametes carry a 1n genome from the newly replicated 8n
694 genome (blue) and adhere to neighbouring erythrocytes (green). (D) 3D intensity plot of SiR-
695 Tubulin staining intensity to reveal dense regions (white dashed line) of axoneme overlap.
696 (E) 3D-sectioned views of exflagellating microgametes, see **Supplementary Video 17** for a
697 3D rotated view. **A-C** Time is depicted as minutes, seconds and milliseconds (mm:ss:ms).
698 Scale bars = 10 μ m. Individual channels of C can be found in **Figure S1E**. All data depicted
699 reflect observations from >10 biological replicates.

700



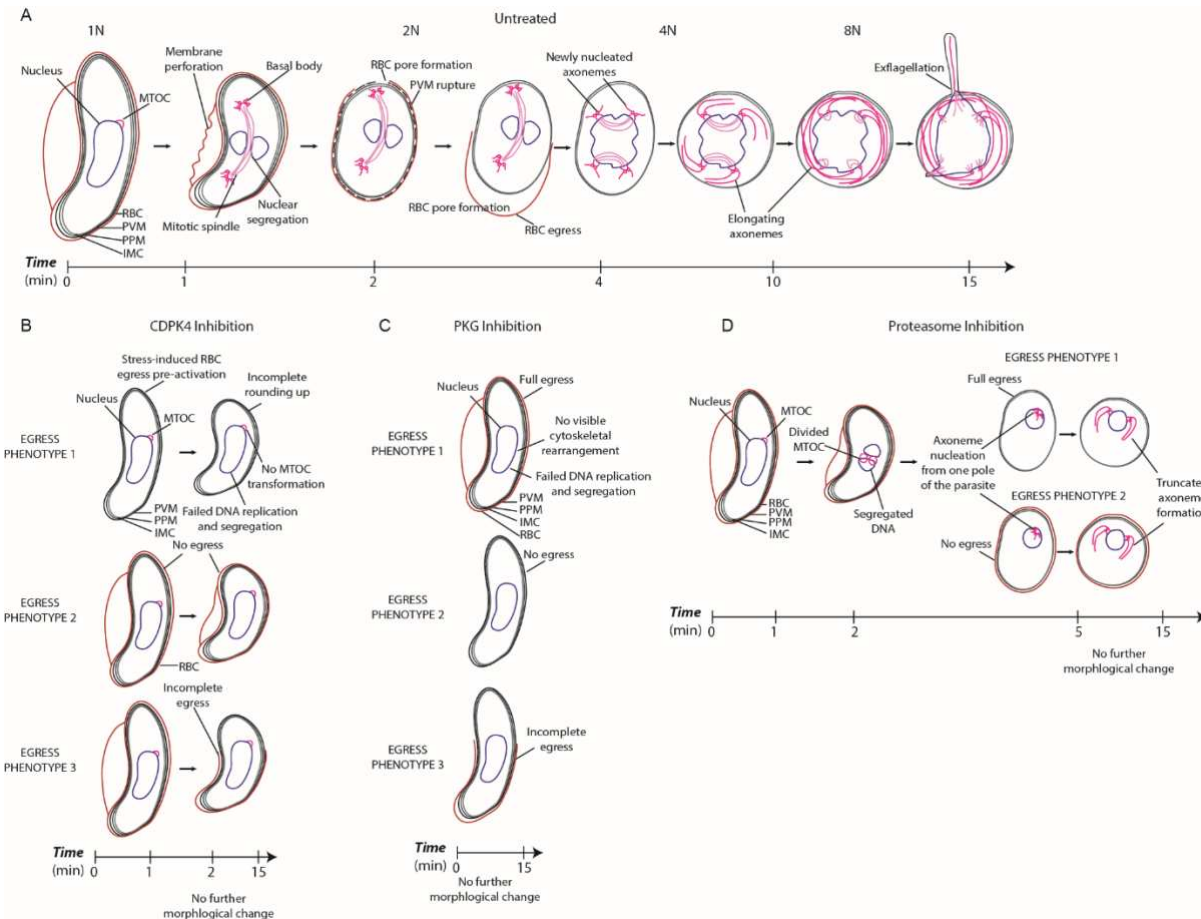
701

702 **Figure 4. Cellular phenotypes of PKG, CDPK4 and proteasome-inhibited parasites**

703 Cellular phenotypes upon inhibition of *P. falciparum* **(A)** CDPK4, **(B)** PKG and **(C)**
 704 proteasome by 1294, ML10 and bortezomib, respectively, during microgametogenesis.
 705 Perturbations to microtubule rearrangement (SiR-Tubulin, magenta), the host erythrocyte
 706 (WGA, green) and DNA replication (Vybrant™ DyeCycle™ Violet, blue) are shown as 2D
 707 maximum intensity projections of 3D data and alongside 3D sectioned views. Individual
 708 channels can be found in **Figure S3**. **(A)** Failed DNA replication, cytoskeletal rearrangement
 709 and MTOC (white dashed line) transformation under 1294-treatment are shown. Stress
 710 induced egress prior to activation is also depicted. See **Supplementary Video 19** for the
 711 corresponding timelapse. **(B)** The failed DNA replication and cytoskeletal rearrangement due
 712 to PKG inhibition by ML10 is shown. Mixed egress phenotypes were observed, including **(i)**
 713 incomplete and **(ii)** failed egress. See corresponding timelapses in **Supplementary Videos**
 714 **23-24**. **(C)** Perturbations to **(i)** MTOC transformation (white dashed line) and **(ii-iii)** formation
 715 of two-three truncated axonemes resulting from proteasome inhibition are shown. See
 716 **Supplementary Videos 25, 27 and 28** for the corresponding timelapses. **(D)** A continuum of
 717 SiR-tubulin staining intensity (arbitrary units) in untreated ($n = 4$), 1294 ($n = 3$), ML10 ($n = 3$)

718 and bortezomib ($n = 6$) treated parasites. **(E)** SiR-tubulin staining (arbitrary units) at 10
719 minutes post-activation under different treatments. Untreated ($n = 14$), 1294 ($n = 16$), ML10
720 ($n = 16$), bortezomib ($n = 9$). Significance was calculated with an unpaired, two-tailed t test;
721 ** $p < .01$, **** $p < .0001$. **(F)** Vybrant™ DyeCycle™ Violet staining (arbitrary units) was
722 significantly reduced (unpaired, two-tailed t test; **** $p < .0001$) at 10 minutes post-activation
723 under different treatments. Untreated ($n = 17$), 1294 ($n = 15$), ML10 ($n = 9$), bortezomib ($n =$
724 16). **(G)** A graph depicting the cell circularity and SiR-tubulin staining intensity of individual
725 cells across the entirety of microgametogenesis under varying treatments. Untreated ($n =$
726 188), 1294 ($n = 58$), ML10 ($n = 106$), bortezomib ($n = 105$). **(H)** Percentage egress at 10
727 minutes post-activation under different treatments was quantified, with distinct egress
728 phenotypes depicted beside the stacked bar graph. Untreated ($n = 58$), 1294 ($n = 20$), ML10
729 ($n = 25$), bortezomib ($n = 24$). All imaging data depicted reflect observations from >3
730 biological replicates.

731



732

733 **Figure 5. Novel insights into microgametogenesis with and without drug inhibition**

734 Schematic diagrams showing the transformations observed by 4D live-cell fluorescence
 735 microscopy of microgametogenesis. The observations depicted are of **(A)** untreated, **(B)**
 736 CDPK4-inhibited, **(C)** PKG-inhibited and proteasome-inhibited microgametocytes, treated
 737 with DMSO, 1294, ML10 and bortezomib, respectively. **(A)** Perforation and pore-formation of
 738 the host cell membrane was found to occur during egress of untreated microgametocytes,
 739 which ejected from a single spindle pole of the parasite. Nuclear segregation was found to
 740 occur perpendicularly to the mitotic spindle. **(B)** CDPK4 inhibition prevented MTOC
 741 transformation and full rounding-up with three distinct egress phenotypes: 1) stress-induced
 742 egress prior to activation, 2) no egress and 3) incomplete egress. **(C)** Inhibition of PKG
 743 prevented rounding-up and any microtubule polymerisation, with 3 distinct egress
 744 phenotypes: 1) no egress, 2) full egress and 3) incomplete egress. **(D)** Proteasome inhibition
 745 resulted in abhorrent MTOC division and some nuclear segregation, with few truncated
 746 axonemes nucleating from one pole of the transformed parasite. Rounding-up of
 747 proteasome-inhibited parasites was observed.